Solar and solar wind energy drivers for O^+ and O_2^+ ion escape at Mars

N. R. Schnepf[1], Y. Dong[1], D. Brain[1], K. G. Hanley[2], W. K. Peterson[1], R. J. Strangeway[3], E. M. B. Thiemann[1], J. S. Halekas[4], J. R. Espley[5], F. Eparvier[1], J. P. McFadden[2]

[1]Laboratory for Atmospheric and Space Physics, University of Colorado Boulder, Boulder, CO, USA
[2]Space Sciences Laboratory, University of California Berkeley, Berkeley, CA, USA
[3]Institute of Geophysics and Planetary Physics, and Department of Earth, Planetary, and Space, University of California Los Angeles, Los Angeles, CA, USA
[4]Department of Physics and Astronomy, University of Iowa, Iowa City, IA, USA
[5]NASA Goddard Space Flight Center, Greenbelt, MD, USA

Key Points:

- Increased solar wind electromagnetic energy flux increases escape of O^+ and O_2^+.
- O^+ and O_2^+ have increased escape rates with increased solar wind kinetic energy.
- Unclear dependence on increased solar irradiance for O^+ and O_2^+ escape.

Corresponding author: Neesha R. Schnepf, `neesha.schnepf@lasp.colorado.edu`

Abstract

Mars once had a dense atmosphere enabling liquid water existing on its surface, however, much of that atmosphere has since escaped to space. We examine how incoming solar and solar wind energy fluxes drive escape of atomic and molecular oxygen ions (O^+ and O_2^+) at Mars. We use MAVEN data to evaluate ion escape from February 1, 2016 through May 25, 2022. We find that Martian O^+ and O_2^+ both have increased escape flux with increased solar wind kinetic energy flux and this relationship is generally logarithmic. Increased solar wind electromagnetic energy flux also corresponds to increased O^+ and O_2^+ escape flux, however, increased solar wind electromagnetic energy flux seems to first dampen ion escape until a threshold level is reached, at which point ion escape increases with increasing electromagnetic energy flux. Increased solar irradiance (both total and ionizing) does not obviously increase escape of O^+ and O_2^+. Our results suggest that the solar wind electromagnetic energy flux should be considered along with the kinetic energy flux as an important driver of ion escape, and that other parameters should be considered when evaluating solar irradiance's impact on O^+ and O_2^+ escape.

Plain Language Summary

Mars was once like Earth with a dense atmosphere enabling liquid water to exist on its surface. However, in the billions of years since then, Mars has lost much of its atmosphere to space. We study how energy inputs from the Sun and from the solar wind can drive escape of the ionized constituents of water from Mars' atmosphere. Ion escape is one of several processes of atmospheric loss, and it is a particularly effective process for removing species heavier than hydrogen and helium from terrestrial atmospheres. We find that previously unconsidered energy fluxes may play an important role in driving ion escape.

1 Introduction

Atmospheric escape may be more efficient at Mars than at Earth or Venus, since Mars is the least massive of the three planets and a weaker gravitational potential leads to a lower escape energy for atmospheric particles. Additionally, without a global magnetic field the solar wind can more directly interact with Mars' atmosphere. This is believed to play a critical role in the escape of planetary ions from Mars' atmosphere (D. Brain et al., 2016). Studying ion escape at Mars is motivated by evidence that early Mars had enough atmospheric pressure to enable liquid water to exist on its surface, whereas present day Mars' atmospheric pressure is only about 0.6% that of Earth's (Pollack et al., 1987; Jakosky & Phillips, 2001).

Atmospheric ion escape is one of several processes that result in atmospheric loss. Ion escape is a particularly effective process for removing species heavier than hydrogen and helium from terrestrial atmospheres (e.g. D. Brain et al. (2016, 2017); Ramstad and Barabash (2021)). For decades now, there has been much effort towards determining the relationship between Mars' atmospheric ion escape and incoming solar and solar wind conditions (for example, see, Lundin et al. (1989, 1990); Nilsson et al. (2010); Ramstad et al. (2015); Y. Dong et al. (2017); Dubinin, Fraenz, Pätzold, McFadden, Mahaffy, et al. (2017); Dubinin, Fraenz, Pätzold, McFadden, Halekas, et al. (2017); Nilsson et al. (2021); Y. Dong et al. (2022)). Solar wind kinetic energy, in the form of solar wind dynamic pressure, and solar ionizing irradiation (typically determined from extreme ultraviolet observations) are the two most studied incoming energy sources for Martian atmospheric ion escape. While studies have considered upstream solar wind magnetic field strength (e.g. Nilsson et al. (2010)), or local crustal magnetic field strength (e.g. Weber et al. (2021)), no previous study has examined the role of the incoming solar wind electromagnetic field energy flux (i.e. the solar wind Poynting flux). Additionally, influences of total solar irradiance variability have mostly been considered in studies of Mars' neutral hydrogen

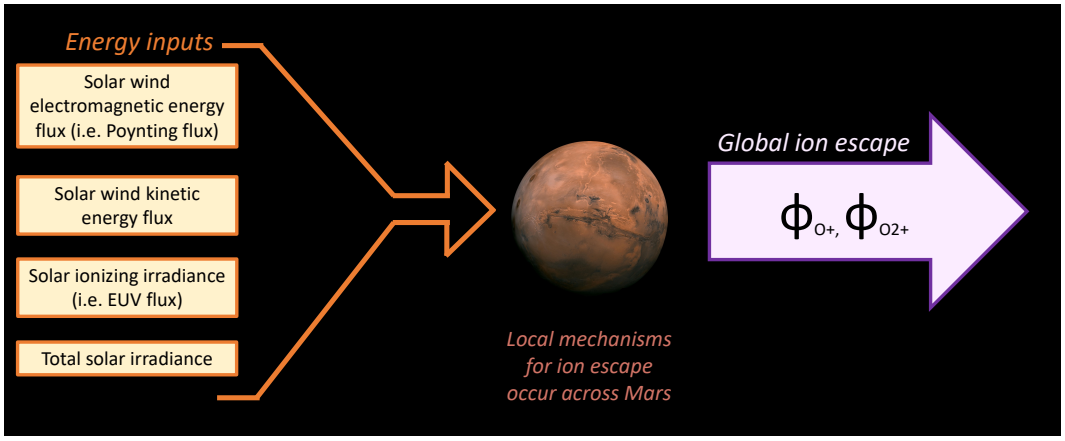

Figure 1. Overview of our study's aim: how does incoming solar and solar wind energy drive global ion escape for O^+ and O_2^+?

exosphere (e.g. Bhattacharyya et al. (2015); J. Halekas (2017)), but not in studies of escaping ions.

Here, we examine how incoming solar and solar wind energy fluxes drive escape of atomic and molecular oxygen ions (O^+ and O_2^+). Our goal is to determine how the escape of O^+ and O_2^+ ions depends on solar and solar wind energy inputs at Mars. As illustrated in Figure 1, energy is input to the Mars system from the Sun (i.e. the solar ionizing irradiance and total solar irradiance) and from the solar wind (i.e. the kinetic energy flux and the electromagnetic energy flux, also known as the Poynting flux). These solar energy inputs drive a multitude of mechanisms local to Mars' magnetosphere that lead to ion escape (e.g. plasma waves, electric field forces, collisions, sputtering; for example, see Ergun et al. (2006)). However, our question is global in nature: how do Mars' global ion escape rates depend on each solar and solar wind energy input? By comparing incoming solar and solar wind energy fluxes with Mars' global O^+ and O_2^+ flux rates, we aim to provide results that may be easily compared against other planets (e.g. how do O^+/O_2^+ flux rates instead depend on these drivers at Earth, Venus, or an exoplanet?)

2 MAVEN Ion Flux Observations

Data from the Mars Atmosphere and Volatile Evolution (MAVEN) mission's SupraThermal and Thermal Ion Composition (STATIC) instrument were used. STATIC measures the in situ distribution of ions as a function of energy (0.1 eV – 30 keV; dE/E∼15%), mass (1024 bins; 1– $\sim$ 100 AMU), direction (360° × 90° field of view), and time (4s resolution) (McFadden et al., 2015).

Ion flux observations from February 1, 2016 through to May 25, 2022 were selected from either MAVEN STATIC d1 or d0 data. These data products only differ in their temporal resolution: d0 samples data as fast as every 32 seconds, whereas d1 has a sampling resolution reaching down to every 4 seconds. Both of these data products include 32 energy channels and 8 mass channels, as well as 4 polar angles (with 11.1 degrees resolution in each direction) and 16 azimuthal angles (of 22.5 degrees resolution). We prioritized using d1 data and used d0 whenever d1 was unavailable. While MAVEN reached Mars in November 2014, we use STATIC data starting in February 2016 because this is when STATIC data started including key background and directional corrections.

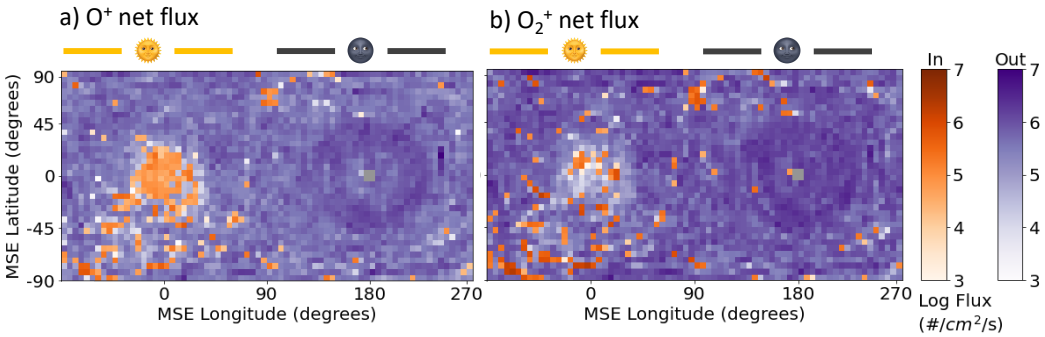

Figure 2. The average observed outwards (purple) and inwards (orange) net flux for O^+ and O_2^+ from February 1, 2016 to May 21, 2022. The data is binned onto a Mars Solar Electric grid; the day- side and night-side of Mars are denoted accordingly.

Following the methods of D. A. Brain et al. (2015), we select observations when MAVEN was located within the spherical shell centered on Mars between 1.25 and 1.45 R_M (i.e. an altitude range of 850-1530 km). Our study focuses on O^+ and O_2^+. We limit STATIC data to those species by using specific mass and energy channels. For O^+ and O_2^+, to avoid ion suppression issues (i.e. localized changes in electric potential on the STATIC electrostatic analyzer surface that limit STATIC's ability to accurately measure low energy ions; see Fowler et al. (2022) for more details), we use the same energy range ($\geq$6 eV) as Y. Dong et al. (2017). This captures most O^+ and O_2^+ observations above Mars' escape energy.

Of course, STATIC cannot observe the entire distribution of plasma, it is limited in its field of view, and it is difficult for us to correct what may be missing. Thus, we are implicitly assuming that STATIC does see the bulk of the distribution, and that what is missing will not be beyond the standard deviation of what is observed. Because the orientation of STATIC with respect to Mars varies on every orbit, it is reasonable to assume that across the thousands of orbits considered, we have captured the average ion inflow and outflow.

The ion fluxes are calculated from observations of ion density and ion velocity. The ion velocity is corrected for spacecraft velocity, as well as for background straggling protons (Hanley, 2023), and for the spacecraft electric potential (Fowler et al., 2022). Ion fluxes are first determined in STATIC instrument coordinates, and then translated from that to Mars Solar Electric (MSE) coordinates. MSE coordinates are defined such that $\hat{x}$ points from Mars to the Sun, $\hat{z}$ is parallel to the solar wind's electric field, and the $\hat{y}$ direction then completes the orthogonal system.

We mapped the radial component of all ion flux observations into a $5^\circ \times 5^\circ$ spatial grid on our spherical surface. Figure 2 shows the average observed outwards and inwards ion fluxes for each species across this MSE global grid and across the entire duration of our study. Overall, both O^+ and O_2^+ see their largest inwards signal on the dayside of Mars, especially in the southern hemisphere, where there are more crustal magnetic fields as compared to the northern hemisphere. The most significant outwards flux is on the night-side. This outwards flux is evenly distributed across both hemispheres and centered around the magnetotail (C. Dong et al., 2015).

3 Solar and Solar Wind Energy Fluxes

We determine Mars' incoming solar wind energy fluxes using data from MAVEN's magnetometer (Connerney et al., 2015) and Solar Wind Ion Analyzer (SWIA; J. S. Halekas et al. (2015)). We use these instruments' observations upstream of Mars' bow shock (J. S. Halekas et al., 2017) to calculate the incoming kinetic energy flux and electromagnetic (EM) energy flux. Solar wind kinetic energy flux has mostly been studied in the form of solar wind dynamic pressure (Lundin et al., 2008; Dubinin, Fraenz, Pätzold, McFadden, Halekas, et al., 2017; Ramstad et al., 2018; Dubinin et al., 2021; Nilsson et al., 2021).

We calculate the kinetic energy flux ($\mathbf{K}$) from SWIA's observed solar wind dynamic pressure ($\mathbf{p}$) and solar wind ion velocity ($\mathbf{v}$):

$$|\mathbf{K}| = \frac{1}{2}|\mathbf{p}||\mathbf{v}| \ . \tag{1}$$

Meanwhile, solar wind electromagnetic energy flux can be decomposed into direct current (DC) and alternating current (AC; also known as Alfvén Poytning flux) contributions. Lennartsson et al. (2004) examined the role of incoming solar wind energy on ion escape at Earth, and chose to simply use the DC EM energy flux. We follow their convention because the AC Poynting flux is more challenging to calculate since it involves band-pass filtering the upstream data and this data is not collected consistently throughout the mission. This is evident in Figure 3, which shows the time series of solar wind kinetic and EM energy fluxes, as well as the gaps in their observations.

The DC solar wind EM energy flux is given as:

$$\mathbf{S} = \frac{1}{\mu_0}\mathbf{E} \times \mathbf{B}, \tag{2}$$

where μ_0 is the vacuum magnetic permeability, $\mathbf{B}$ is the solar wind magnetic field (measured by MAVEN's magnetometer, and also known as the interplanetary magnetic field [IMF]), and $\mathbf{E}$ is the solar wind electric field. Instead of using direct measurements of $\mathbf{E}$, similar to Lennartsson et al. (2004), we use the substitution $\mathbf{E} = -\mathbf{v} \times \mathbf{B}$ to obtain:

$$\mathbf{S} = -\frac{1}{\mu_0}(\mathbf{v} \times \mathbf{B}) \times \mathbf{B}. \tag{3}$$

As seen in Figure 3, the solar wind EM energy flux predominantly ranges from 10^{-4} to 10^{-2} mW/m^2, whereas the kinetic energy flux spans 10^{-2} to 1 mW/m^2.

For solar irradiance, we consider both the Sun's ionizing irradiance and the total solar irradiance at Mars. For solar ionizing irradiance, we use MAVEN's extreme ultraviolet monitor (EUVM; Eparvier et al. (2015)) and the Flare Irradiance Spectral Model-Mars (FISM-M; Thiemann et al. (2017)). For each MAVEN orbit, we integrate from 0 to 91 nm to obtain the solar ionizing irradiance for our focus ion species (O^+ and O_2^+) (Schunk & Nagy, 2009). The time series of ionizing irradiance is depicted in Figure 3 with the orange line.

We also consider the total solar irradiance (TSI) at Mars since non-ionizing irradiance plays an indirect role in ion escape, and ionizing irradiance is a small fraction of the TSI. We obtain Mars' TSI by using the mean value at Earth (1361 W/m^2) (Dudok de Wit et al., 2017), and then using Earth's and Mars' distances from the Sun to calculate the TSI at Mars. The TSI time series is illustrated in Figure 3 with the red line. Note that ionizing irradiance typically exceeds the solar wind energy fluxes, however, it is a small fraction of the total solar irradiance.

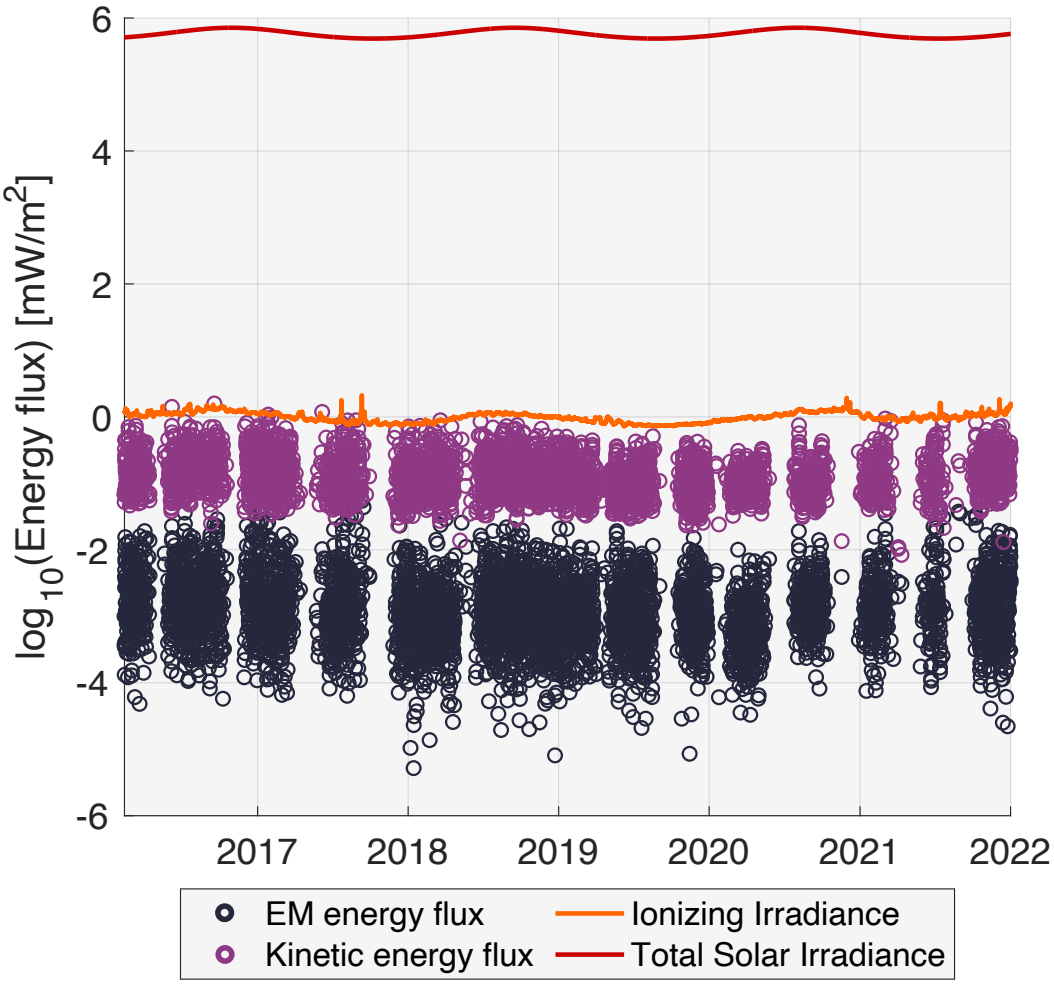

Figure 3. Time series of the considered solar wind and solar energy fluxes. Black circles: solar wind electromagnetic energy flux. Magenta circles: solar wind kinetic energy flux. Orange line: solar ionizing irradiance. Red line: total solar irradiance. Gaps in solar wind energy flux observations are due to times when MAVEN was not sampling the solar wind.

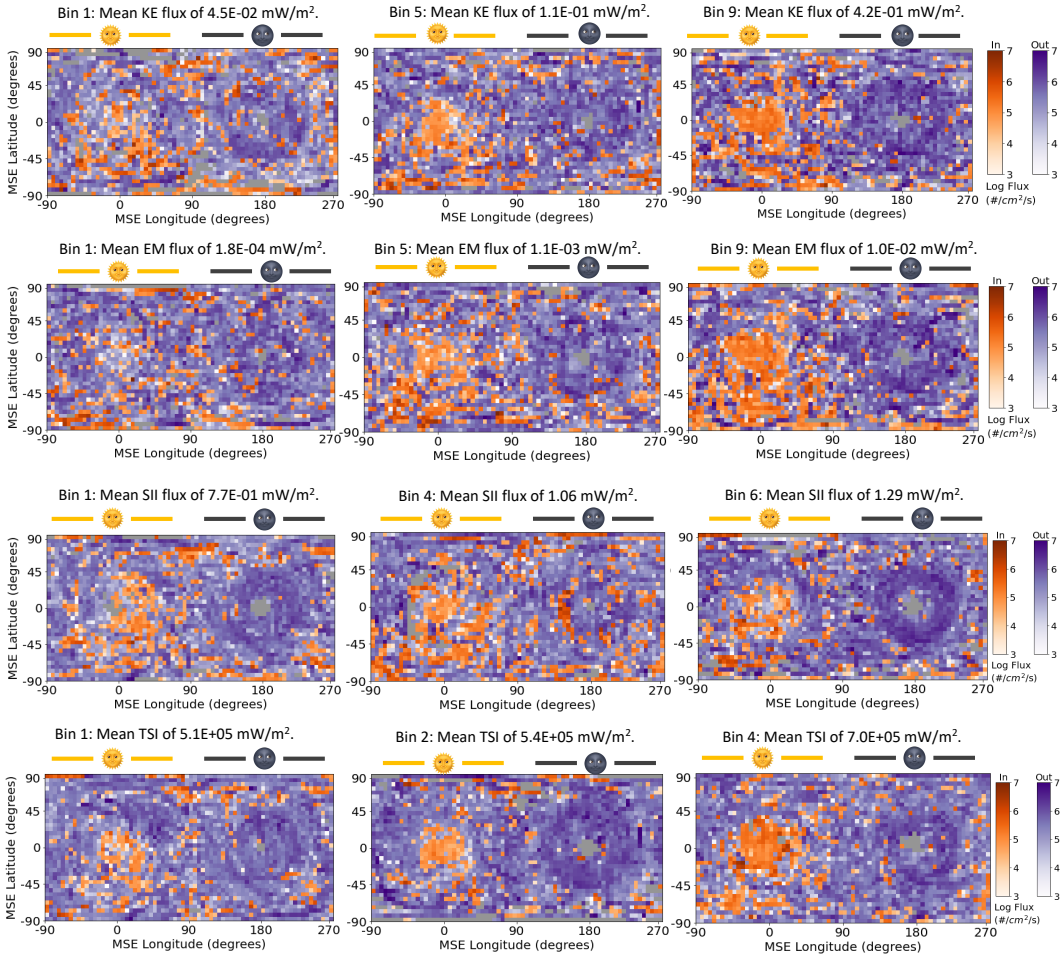

Figure 4. The average observed outwards (purple) and inwards (orange) net flux for O^+ for each energy input (KE: solar wind kinetic energy flux, EM: solar wind electromagnetic energy flux, SII: solar ionizing irradiance, TSI: total solar irradiance) and the low, medium, and high value bins for that energy source. The data is binned onto a Mars Solar Electric grid; the day-side and night-side of Mars are denoted accordingly.

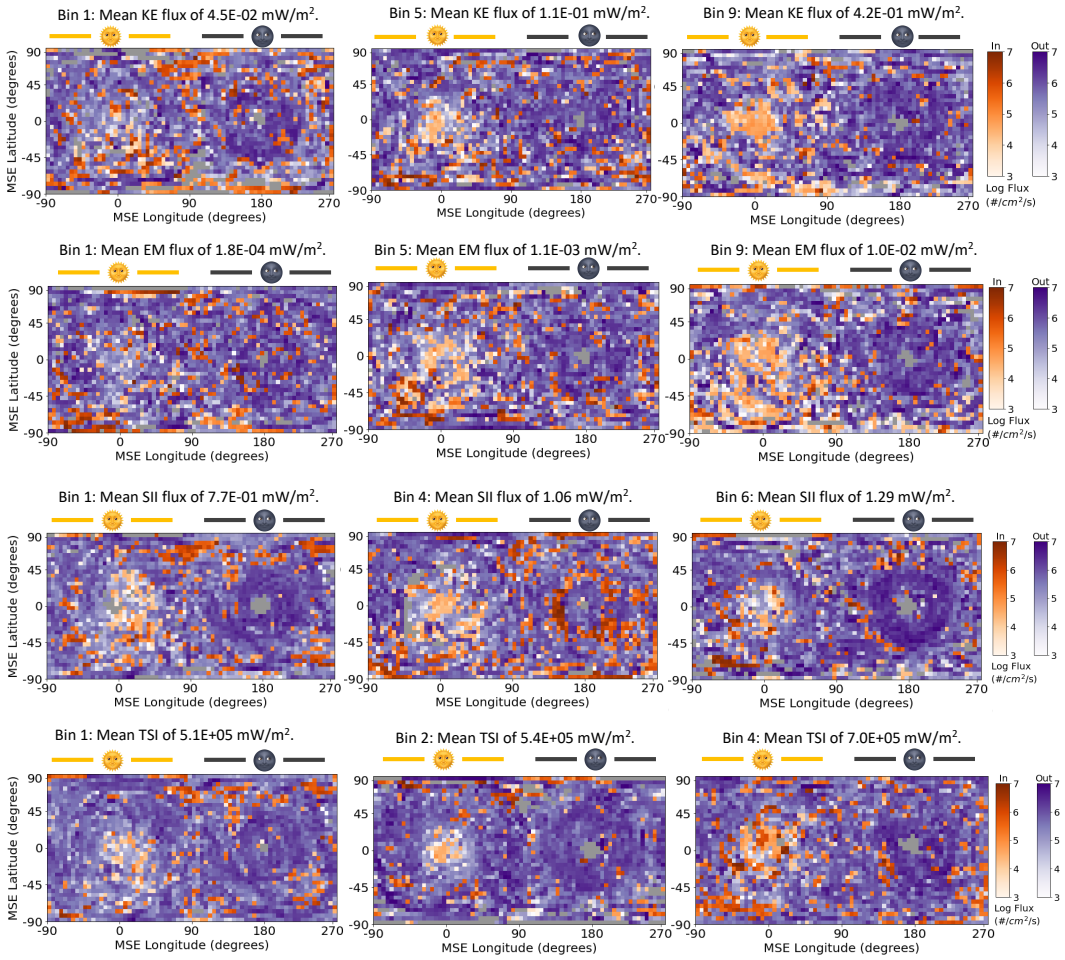

Figure 5. The average observed outwards (purple) and inwards (orange) net flux for O_2^+ for each energy input (KE: solar wind kinetic energy flux, EM: solar wind electromagnetic energy flux, SII: solar ionizing irradiance, TSI: total solar irradiance) and the low, medium, and high value bins for that energy source. The data is binned onto a Mars Solar Electric grid; the day-side and night-side of Mars are denoted accordingly.

4 Comparing ion escape to the incoming solar and solar wind energy drivers

All ion flux observations were paired to their nearest-in-time solar and solar wind driver observations. Marquette et al. (2018) showed that solar wind speed and magnetic field generally stay coherent through the duration of a MAVEN orbit ($\sim$ 4.5 hours). Thus, in our analysis if the nearest-in-time upstream observation exceeded a time difference of 4.5 hours, the ion flux observation was discarded. It is possible for upstream conditions to change dramatically within one orbit during extreme events, however, because the global ion flux is compared to binned upstream conditions (described in the next paragraphs), we minimize this error.

After pairing ion flux observations to upstream energy inputs, for each driver, the ion flux observations were ranked by ascending driver value. Then, the ion flux data were binned such that each bin had an equivalent number of observations. For the solar wind energy fluxes, $\sim$200,000 observations per bin provided adequate data coverage across the planet and led to a total of 9 bins of different driver average value. The top two rows of Figures 4-5 shows the spatial distributions of the lowest value, middle value, and highest value solar wind energy flux bins. Supplementary Figures S1 and S2 shows the data density for each solar wind energy flux bin's ion flux observations.

Ranking the data by solar irradiance led to significant biases in the spatial coverage. This is largely because MAVEN's orbit varies with the season and solar irradiance is a seasonal signal. Thus, for ionizing irradiance to have coverage equivalent to the solar wind drivers, we needed $\sim$300,000 observations per bin, which leads to 6 bins. The third row in both Figures 4-5 shows the spatial distribution of ion flux observations for solar ionizing irradiance. Supplementary Figure S3 shows the data density for each ionizing irradiance bin. Meanwhile, for TSI, the spatial bias was more extreme and $\sim$500,000 observations per bin were instead needed. This led to only 4 bins of different average TSI. The bottom row in Figures 4-5 shows the spatial distribution of ion flux observations for TSI. Supplementary Figure S4 shows their data density. Table 1 specifies the number of observations included in each driver's bin.

For each energy driver's ion flux bin, we calculated the average global net radial ion flux for each species. Figure 6 shows each bin's global net ion flux for each driver. In each scatter plot, the horizontal whiskers show the standard deviation in the upstream driver's bin values and the vertical whiskers correspond to the statistical error in the global ion flux average. This error was calculated using the standard deviation of each grid cell's ion flux observations (i.e. σ_i is the standard deviation of the ith grid cell), propagated to the global average ion flux value as follows:

$$\triangle\Phi = \sqrt{w_1^2\sigma_1^2 + w_2^2\sigma_2^2 + \ldots + w_i^2\sigma_i^2}, \tag{4}$$

where the weights w correspond to how each ion flux bin's relative surface area is considered:

$$w = \frac{\text{grid cell surface area}}{\text{grid total observed surface area}}. \tag{5}$$

Figure 6 shows best fit lines for each ion flux driver comparison; Table 1 gives the equations and r-squared values for these best fit lines. Because the ion flux was plotted on a logarithmic scale, the equations are relating the various drivers to the logarithmic ion flux. For the solar wind electromagnetic energy flux, the energy flux was also handled in a logarithmic scale to better view the orders of magnitude differences. The goal of the best fit lines was to capture each plot's trend in the simplest way possible for easier comparison with other studies.

Figure 7 explores the mutual correlations of the solar and solar wind energies considered here. Unsurprisingly, there is significant mutual correlation between the solar wind

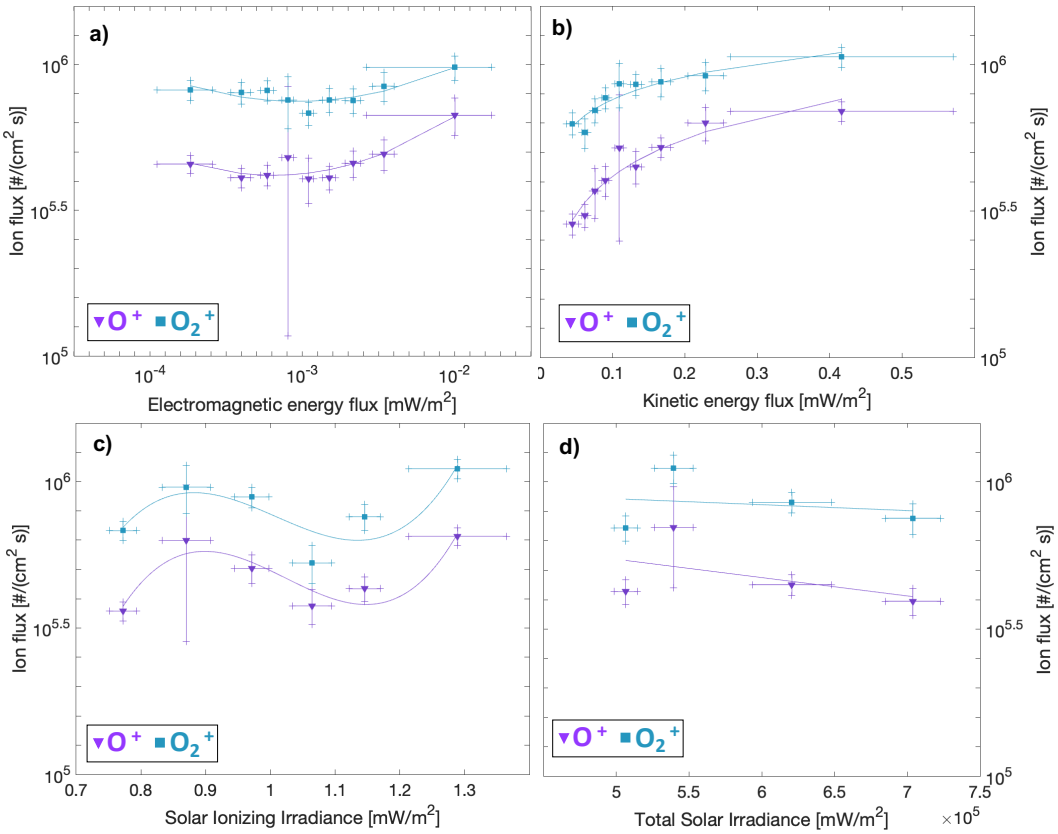

Figure 6. The global net ion flux for each solar and solar wind energy driver and for each ion species (purple triangles: O^+, blue squares: O_2^+). The horizontal whiskers denote the standard deviation of the bin's energy flux values and the vertical whiskers mark the ion flux statistical error. Solid lines depict the best fit equations shown in Table 1. The top row shows ion flux versus a) solar wind electromagnetic energy flux and b) solar wind kinetic energy flux. The next row shows ion flux versus c) solar ionizing irradiance and (d) total solar irradiance.

kinetic energy flux and solar wind electromagnetic energy flux, as well as between solar ionizing irradiance and total solar irradiance. For the solar wind energy fluxes, this mutual correlation largely arises because both the kinetic energy flux and EM energy flux are calculated using solar wind proton velocities. Thus, along with exploring the correlation of each energy driver and ion flux, we also deep-dive into the influence of solar wind proton velocities versus the IMF amplitude (Section 4.3).

4.1 Solar Wind Electromagnetic Energy Flux

Figure 6a shows global ion flux versus solar wind EM energy flux. The oxygen ion species (O^+: purple triangles, O_2^+: blue squares) both have increased ion escape with increased solar wind DC EM energy flux, with a general trend best described using a quadratic equation. Table 1 shows the best fit equation illustrated in the figure, as well as its fairly strong r^2 correlation value. It is interesting that the general trend is quadratic: for both O^+ and O_2^+ increasing EM energy flux causes the net ion flux (which is outwards) to slightly diminish, then seemingly at a tipping point, the ion flux increases with increased solar wind EM energy flux. The quadratic coefficient's 95% confidence bounds are all above zero for both O^+ and O_2^+, indicating that this turn is a real feature. Discussed more in

Table 1. Comparing ion escape for O^+ and O_2^+ to incoming solar and solar wind energy fluxes. For each incoming energy flux, the number of observations per bin, the best fit equation, and the r^2 correlation coefficient are given. This information is also given for the solar wind velocity and interplanetary magnetic field.

		Solar Wind Electromagnetic Energy Flux	
	# obs per bin	Best fit equation	r^2
O^+	217254	$\log O^+(\log x) = 0.14(\log x)^2 + 0.90 \log x + 7.0$	0.87
O_2^+	217254	$\log O_2^+(\log x) = 0.11(\log x)^2 + 0.66 \log x + 6.9$	0.75
		Solar Wind Kinetic Energy Flux	
	# obs per bin	Best fit equation	r^2
O^+	217254	$\log O^+(x) = 6.0 + 0.18x$	0.92
O_2^+	217254	$\log O_2^+(x) = 6.1 + 0.11x$	0.88
		Solar Wind Velocity	
	# obs per bin	Best fit equation	r^2
O^+	217254	$\log O^+(x) = 8.8 \times 10^{-3}x + 5.3$	0.77
O_2^+	217254	$\log O_2^+(x) = 4.2 \times 10^{-6}x^2 - 2.9 \times 10^{-3}x + 6.4$	0.73
		Interplanetary Magnetic Field	
	# obs per bin	Best fit equation	r^2
O^+	217254	$\log O^+(x) = 0.01x^2 - 0.07x + 5.7$	0.56
O_2^+	217254	$\log O_2^+(x) = 0.01x^2 - 0.08x + 6.0$	0.51
		Solar Ionizing Irradiance	
	# obs per bin	Best fit equation	r^2
O^+	325882	$\log O^+(x) = 23.5x^3 - 72.2x^2 + 72.8x - 18.4$	0.86
O_2^+	325882	$\log O_2^+(x) = 20.2x^3 - 61x^2 + 60.5x - 13.8$	0.70
		Total Solar Irradiance	
	# obs per bin	Best fit equation	r^2
O^+	488822	$\log O^+(x) = -6.2 \times 10^{-7}x + 6.0$	0.24
O_2^+	488822	$\log O_2^+(x) = -2.0 \times 10^{-7}x + 6.0$	0.04

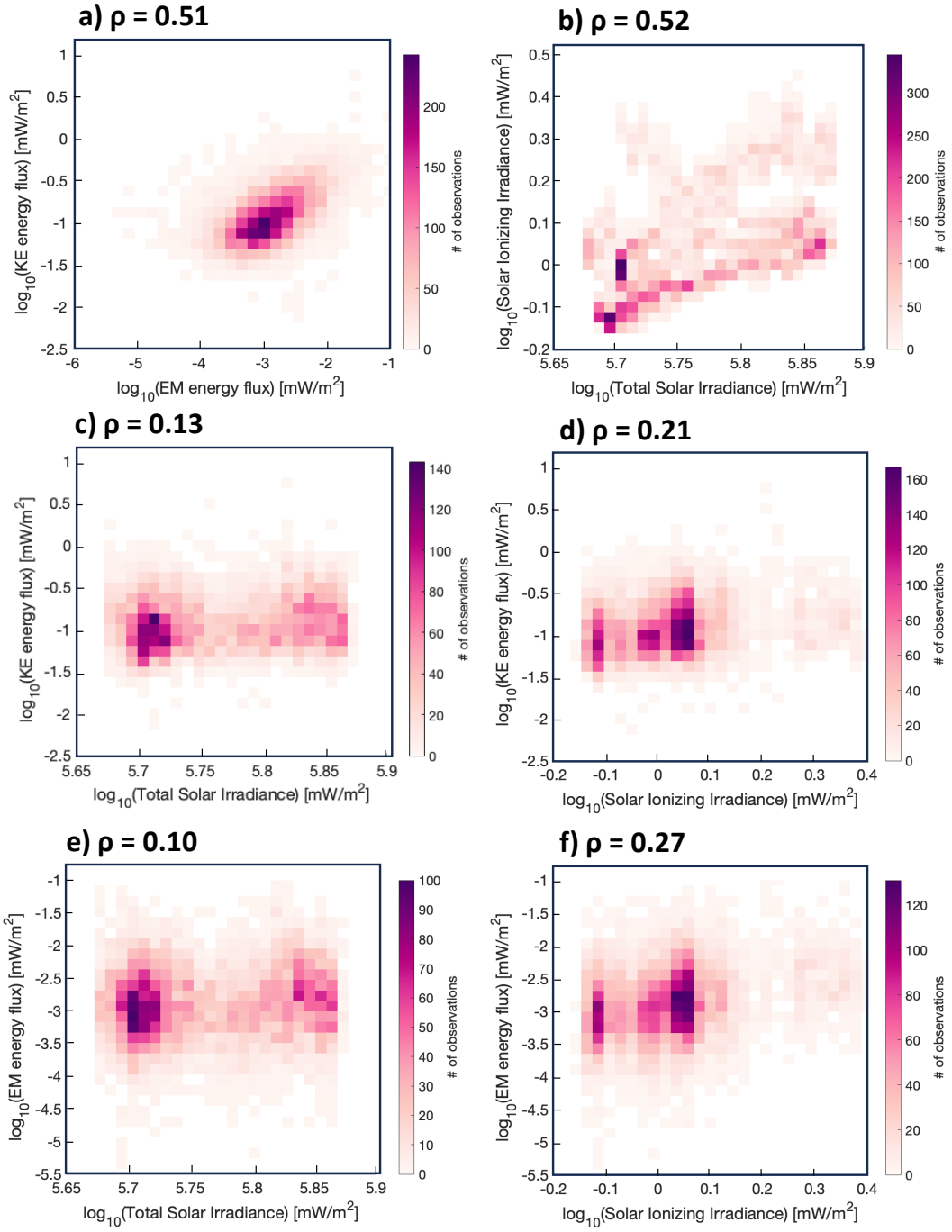

Figure 7. The mutual correlation of each solar and solar wind energy source is shown here in observation heat maps. Each data pair's Pearson correlation coefficient is shown on the plot (higher numbers denote larger correlation). a) Solar wind kinetic energy flux versus electromagnetic energy flux. b) Solar ionizing irradiance versus total solar irradiance. c) Solar wind kinetic energy flux versus total solar irradiance. d) Solar wind kinetic energy flux versus solar ionizing irradiance. e) Solar wind electromagnetic energy flux versus total solar irradiance. f) Solar wind electromagnetic energy flux versus solar ionizing irradiance.

Section 4.3, the quadratic fit is likely due to the solar wind EM energy flux's dependence on the IMF.

The horizontal whiskers denote the variance in solar wind EM energy flux for a given bin. The rightmost bin has the largest EM energy flux variance since it is sampling the more extreme EM flux values. Future studies should be able to incorporate additional data during the solar cycle maximum to improve the sampling in the most extreme bin.

Figures 4-5 shows the spatial distribution of each species' ion flux for the lowest, middle, and highest solar wind EM flux bins (maps for each bin are shown in Supplementary Figure S6). As the solar wind EM flux increases, outwards ion flux increases on the night side across both hemispheres, however, incoming ion flux on the day side (especially in the southern hemisphere; the hemisphere with strong crustal magnetic fields) also increases. This pattern is consistent for both O^+ and O_2^+, although the inwards ion flux amplitude for O^+ is consistently larger than for O_2^+ (which is why its overall ion flux is consistently smaller in amplitude than O_2^+'s).

The role of solar wind EM flux on ion escape at Mars has not been considered in previous studies. However, this energy source should be considered as a possibly important driver of O^+ and O_2^+ escape. Solar wind energy can be transferred to ions through collisions, or through electromagnetic fields. The trend shown in Figure 6a suggests the dominating local mechanisms shift once a threshold of incoming solar wind EM flux is reached. In Section 4.3 we explore whether this may be caused by the solar wind proton velocity or the interplanetary magnetic field (IMF).

Even though the solar wind EM energy flux is smaller in amplitude than the kinetic energy flux (shown in Figure 3), EM fields may be a more efficient method of transferring energy from the solar wind to ions, especially since EM fields are the dominant method of energy transfer in collisionless plasma (Wang et al., 2024). Future studies could better constrain ion escape's dependency on this driver by utilizing longer time-series of data, as well as performing modelling work to determine what physical processes may be causing the observed dependency on solar wind EM flux for ion escape. Additionally, because there is some mutual correlation between the solar wind's EM energy flux and kinetic energy flux (see Figure 7) due to both parameters depending on solar wind velocity, future studies should consider examining ion flux's dependency on both solar wind kinetic and EM energy fluxes simultaneously.

4.2 Solar Wind Kinetic Energy Flux

Figure 6b shows global ion flux versus solar wind kinetic energy flux. Similar to the solar wind EM energy flux, the rightmost bin has the largest horizontal whiskers because it is sampling the more extreme solar wind kinetic energy conditions and has the largest standard deviation.

Both species show an increase in outwards ion flux with an increase in solar wind kinetic energy. Figures 4-5 shows the spatial distribution of each species' ion flux for the lowest, middle, and highest solar wind kinetic energy flux bins (maps for each bin are shown in Supplementary Figure S5). Similar to the distributions for solar wind EM energy flux bins, as the solar wind kinetic energy flux increases, outwards flux on the night side grows in amplitude, however, inwards flux on the day side's southern hemisphere also grows in amplitude. Overall, the total ion flux is outwards and logarithmically grows in amplitude with increasing solar wind kinetic energy flux.

This matches well with some previous studies (Lundin et al., 2008; Dubinin, Fraenz, Pätzold, McFadden, Halekas, et al., 2017; Dubinin et al., 2021) examining Martian ion escape's dependence on solar wind dynamic pressure (which relates to kinetic energy flux as shown in equation 1). However, there are some studies which found the opposite trend

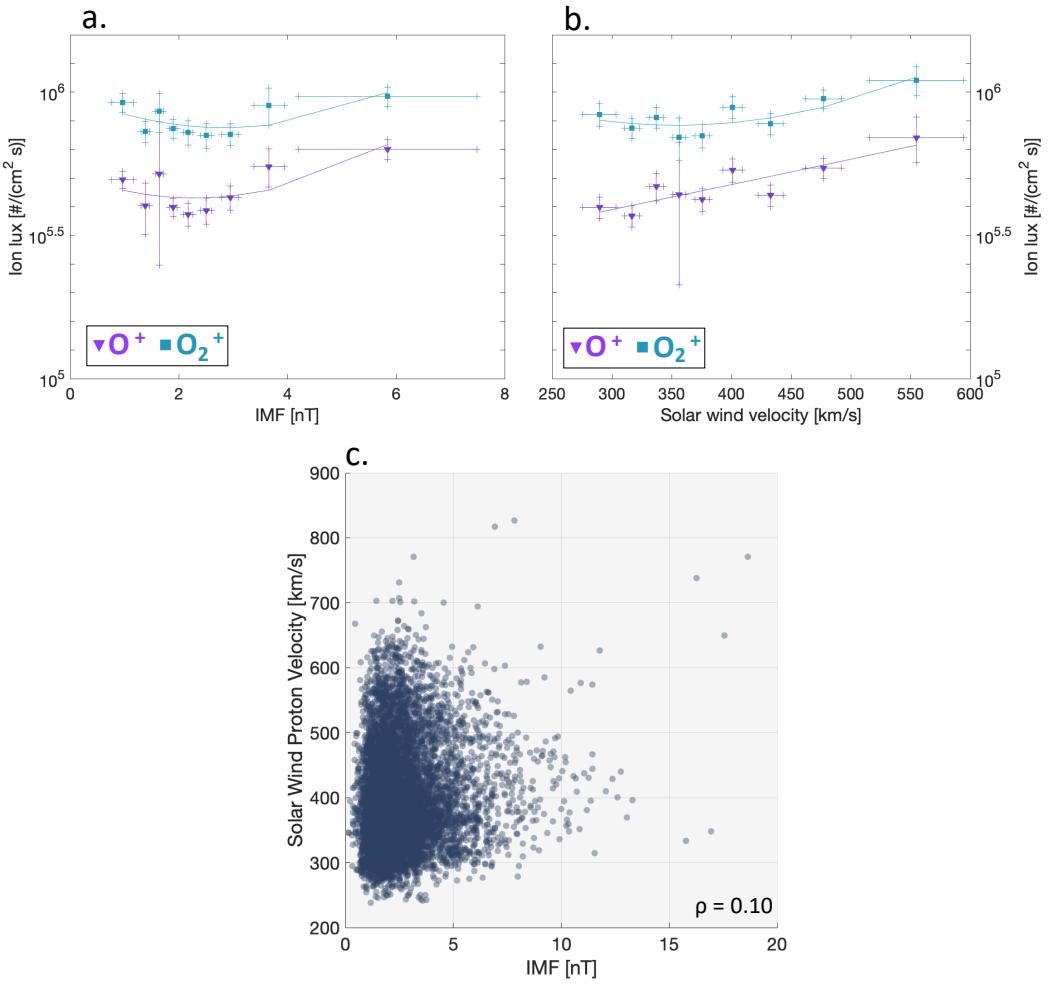

Figure 8. The global net ion flux for a) the interplanetary magnetic field (IMF) and b) the solar wind proton velocity (purple triangles: O^+, blue squares: O_2^+). The horizontal whiskers denote the standard deviation of the IMF or solar wind velocity bin's values and the vertical whiskers mark the ion flux statistical error. Solid lines depict the best fit equations shown in Table 1. The bottom panel (c) shows the mutual correlation of the IMF and solar wind proton velocity. Their Pearson correlation coefficient (ρ = 0.10) is shown on the plot and indicates minimal mutual correlation.

(Ramstad et al., 2018; Nilsson et al., 2021): that ion escape decreases with increasing solar wind dynamic pressure (or increasing kinetic energy flux). These two studies both evaluated solar wind dynamic pressure simultaneously with the solar ionizing irradiance. Like the first set of studies, we do not simultaneously fit for both solar wind kinetic energy and solar ionizing irradiance. Indeed, as shown in Figure 7, solar wind energy fluxes do not seem correlated to solar ionizing irradiance (nor do they seem correlated to TSI). Thus, we decided a simultaneous fit of multiple (ideally, of all four) energy drivers was beyond the scope of this study.

MAVEN is starting to collect data from the current solar maximum. Future studies should utilize data from more of the solar cycle maximum so the extreme-most bin can be separated into multiple bins of higher solar wind kinetic energy flux. Such future studies will be able to answer the question: will the ion escape continue to increase as solar wind kinetic energy flux increases?

4.3 Solar Wind Velocity and Interplanetary Magnetic Field (IMF)

Figure 8a-b shows the global net ion flux versus the solar wind's constituent components of the interplanetary magnetic field (IMF) and solar wind proton velocity. We chose these two parameters because they are used for the previously considered solar wind EM energy flux, and proton velocity is also used for solar wind kinetic energy flux.

Table 1 summarizes the best fit lines shown in these plots. The IMF results have a similar structure to the results for the solar wind's EM energy flux: both show a decrease in ion flux with an initial increase in either the solar wind EM energy flux or the IMF amplitude before the ion flux switches to increasing as the solar wind term also continues to increase. Meanwhile, as the solar wind velocity increases, ion flux mostly increases as well. However, for O^+ the relationship between ion flux and solar wind velocity is different than that for ion flux and solar wind EM or kinetic energy fluxes (i.e., mostly linear versus mostly quadratic or logarithmic). For O_2^+, it is again quadratic, which is similar to the solar wind EM energy flux relationship, rather than the solar wind kinetic energy flux trend.

Figure 8c shows the correlation between the IMF and solar wind proton velocity, with the Pearson correlation coefficient of $\rho = 0.10$. This minimal correlation suggests that the relationship between ion flux and solar wind EM energy is largely due to the IMF, with the solar wind velocity slightly accentuating the quadratic shape of the solar wind EM energy results as compared to results for solely the IMF. Meanwhile, the solar wind kinetic energy flux is due to the solar wind velocity and the solar wind mass density (which is not considered here), however, its shape differs significantly from the solar wind velocity results, indicating the important role solar wind mass density must also play in the total kinetic energy flux's relationship with ion flux.

4.4 Solar Ionizing Irradiance

As described in Section 3, the solar ionizing irradiance is predominantly extreme ultraviolet (EUV) spectra (Thiemann et al., 2017; Eparvier et al., 2015). The binning differs from the solar wind energy fluxes; bins now use over 300,000 observations, yielding six bins rather than nine. The spatial distributions for each species' ion flux in the lowest, middle, and highest solar ionizing irradiance bins are shown in Figures 4-5 (maps for each bin are shown in Supplementary Figure S7). Similar to the spatial distributions for the solar wind energy fluxes, outwards ion flux dominates across both night side hemispheres. However, for solar ionizing irradiance, the day side's inwards ion flux is more spread across both hemispheres. While the ion flux distribution spatially varies across the solar ionizing irradiance bins, there is not an obvious trend.

Figure 6c shows global ion flux versus solar ionizing irradiance. We find that increasing the solar ionizing irradiance overall imperceptibly changes the ion flux for O^+ and O_2^+. Table 1 shows these species' results had a cubic best-fit line. The ion flux in the lowest solar ionizing irradiance bin is smaller than the ion flux of the highest solar ionizing irradiance bin, however, the ion flux of the in-between bins shows a decrease with increased ionizing irradiance.

Our ambiguous results differ from the results of Y. Dong et al. (2017) and Y. Dong et al. (2022). However, those studies have a couple major differences with this study: 1) they constrained ionizing irradiance's influence on ion escape while controlling for other variations in solar wind conditions and 2) they utilized an earlier time period of MAVEN data which included larger amplitudes of solar ionizing irradiance, but included issues with the STATIC ion directions (Fowler et al., 2022; Hanley, 2023). We hope that future studies will be able to take advantage of the next solar maximum so that a wider range of solar ionizing irradiance can be compared to ion fluxes. We also encourage future work to perform a fit of all solar and solar wind drivers simultaneously.

Our results are instead comparable to studies which simply evaluate the influence of solar ionizing irradiance on O^+ and O_2^+ at altitudes similar to our study (e.g. Dubinin, Fraenz, Pätzold, McFadden, Mahaffy, et al. (2017)'s results for altitudes of 850-1530 km). The lack of a simple relationship between ionizing irradiance and oxygen ion fluxes suggests that the increase in oxygen ions within Mars' ionosphere is not directly translating to increased outwards flux. Indeed, modelling studies show Mars' oxygen ions have mixed dependency on ionizing irradiance for escape; whether a study finds increased or decreased O^+/O_2^+ escape with ionizing irradiance depends on what other parameters the study considers (C. Dong et al., 2015; Brecht et al., 2016; Cravens et al., 2017). As Brecht et al. (2016) states, the relation between solar ionizing irradiance and ion flux is very nonlinear.

4.5 Total Solar Irradiance

For total solar irradiance (TSI), the binning differs from the other considered energy fluxes. To avoid spatial biases, bins now use 488,822 ion flux observations, yielding four bins rather than six or nine. The spatial distributions for each species' ion flux in the lowest, middle, and highest TSI bins are shown in Figures 4-5 (maps for each bin are shown in Supplementary Figure S8). Outwards ion flux is always dominant on the night side, inwards ion flux dominant in the day side, especially the southern hemisphere. However, the largest amplitudes of outwards flux occur in the second TSI bin, and otherwise seem unchanged across bins. Meanwhile, inwards flux is largest in bins 3 and 4.

Figure 6d shows the global ion flux versus total solar irradiance. O^+ has large ion flux statistical error in the second bin, suggesting that O^+'s escape flux may stay fairly flat with increased TSI. Like O^+, O_2^+ also has a weakly correlated, flat dependency on TSI. TSI and solar ionizing irradiance are mutual correlated (shown in Figure 7), so future studies may benefit from fitting for both drivers simultaneously. However, the mechanisms in which ionizing irradiance and non-ionizing irradiance drive escape are sufficiently different, and complicated, that future studies might investigate whether other Martian seasonal parameters should be constrained when examining ion escape's dependency on TSI.

5 Conclusions and Outlook

We evaluate solar and solar wind energy drivers for atomic and molecular oxygen ions (O^+ and O_2^+). As shown in Figure 1, our analysis includes both solar wind kinetic energy (considered in dynamic pressure form in several previous studies) and electromagnetic energy (unconsidered in previous studies). We find that as both of these solar wind

energy fluxes increase, there is increased outwards flux of O^+/O_2^+ There is, however, nuance to this as the increase occurs logarithmically for the kinetic energy flux driver, and instead seems to depend on tipping point for the EM energy flux driver. These drivers have some mutual correlation with one another, but the relationship between ion flux and solar wind EM energy flux seems to mostly depend on the IMF.

Along with considering these solar wind energy fluxes, we also evaluate both the much studied solar ionizing irradiance and the less considered total solar irradiance. We find that the escape fluxes of O^+ and O_2^+ lack a clear relationship with both types of solar irradiance. This is likely due to the complicated relationship between both ionizing and non-ionizing irradiance with ion escape.

We strongly encourage future studies determining empirical relationships between Martian O^+ and O_2^+ ion escape and solar drivers to simultaneously consider all of the solar and solar wind energy sources considered here. Further modelling work exploring the possible processes at play for each of these ion species and each of these drivers would also be helpful to understand the underlying physics of the different regimes we observe. And finally, we encourage comparisons to be made examining ion escape's dependency on these solar and solar wind drivers at other planets both within, and beyond, our solar system.

6 Data Availability Statement

MAVEN L2 STATIC data used to create the O^+ and O_2^+ fluxes are publicly available at NASA's Planetary Data System (`https://pds-ppi.igpp.ucla.edu/search/view/?f=yes&id=pds://PPI/maven.static.c`). MAVEN EUVM data used here to calculate the total solar irradiance and total ionizing solar irradiance are also publicly available at NASA's Planetary Data System (`https://pds-ppi.igpp.ucla.edu/search/view/?f=yes&id=pds://PPI/maven.euv.modelled`). The upstream solar wind data used to obtain solar wind electromagnetic and kinetic energy fluxes are publicly available through the University of Iowa (`http://homepage.physics.uiowa.edu/~jhalekas/drivers.html`).

Acknowledgments
This work was supported by the NASA MAVEN project through the Mars Exploration Program.

References

Bhattacharyya, D., Clarke, J. T., Bertaux, J.-L., Chaufray, J.-Y., & Mayyasi, M. (2015). A strong seasonal dependence in the martian hydrogen exosphere. *Geophysical Research Letters*, *42*(20), 8678–8685.

Brain, D., Bagenal, F., Ma, Y.-J., Nilsson, H., & Stenberg Wieser, G. (2016). Atmospheric escape from unmagnetized bodies. *Journal of Geophysical Research: Planets*, *121*(12), 2364–2385.

Brain, D., Barabash, S., Bougher, S., Duru, F., Jakosky, B., & Modolo, R. (2017). Solar wind interaction and atmospheric escape. In *The Atmosphere and Climate of Mars* (pp. 464–496). Cambridge: Cambridge University Press.

Brain, D. A., McFadden, J. P., Halekas, J. S., Connerney, J. E. P., Bougher, S. W., Curry, S., ... Seki, K. (2015). The spatial distribution of planetary ion fluxes near mars observed by maven. *Geophysical Research Letters*, *42*, 9142–9148. doi: 10.1002/2015GL065293.

Brecht, S. H., Ledvina, S. A., & Bougher, S. W. (2016). Ionospheric loss from mars as predicted by hybrid particle simulations. *Journal of Geophysical Research: Space Physics*, *121*(10), 10–190.

Connerney, J. E. P., Espley, J., Lawton, P., Murphy, S., Odom, J., Oliversen, R., &

Sheppard, D. (2015). The maven magnetic field investigation. *Space Science Reviews*, *195*(1-4), 257–291. doi: 10.1007/s11214-015-0169-4

Cravens, T. E., Hamil, O., Houston, S., Bougher, S., Ma, Y., Brain, D., & Ledvina, S. (2017). Estimates of ionospheric transport and ion loss at mars. *Journal of Geophysical Research: Space Physics*, *122*(10), 10–626.

Dong, C., Bougher, S. W., Ma, Y., Toth, G., Lee, Y., Nagy, A. F., ... Najib, D. (2015). Solar wind interaction with the martian upper atmosphere: Crustal field orientation, solar cycle, and seasonal variations. *Journal of Geophysical Research: Space Physics*, *120*(9), 7857–7872.

Dong, Y., Brain, D., Ramstad, R., Fang, X., McFadden, J., Halekas, J., ... Jakosky, B. (2022). The dependence of martian ion escape on solar euv irradiance as observed by maven. *Icarus*, 115288. doi: 10.1016/j.icarus.2022.115288

Dong, Y., Fang, X., Brain, D. A., McFadden, J. P., Halekas, J. S., Connerney, J. E. P., ... Jakosky, B. M. (2017). Seasonal variability of martian ion escape through the plume and tail from maven observations. *Journal of Geophysical Research: Space Physics*, *122*, 4009-4022. doi: 10.1002/2016JA023517

Dubinin, E., Fraenz, M., Pätzold, M., McFadden, J., Halekas, J. S., DiBraccio, G. A., ... Zelenyi, L. (2017). The effect of solar wind variations on the escape of oxygen ions from mars through different channels: Maven observations. *Journal of Geophysical Research: Space Physics*, *122*, 11,285–11,301. doi: 10.1002/2017JA024126

Dubinin, E., Fraenz, M., Pätzold, M., McFadden, J., Mahaffy, P. R., Eparvier, F., ... Zelenyi, L. (2017). Effects of solar irradiance on the upper ionosphere and oxygen ion escape at mars: Maven observations. *Journal of Geophysical Research: Space Physics*, *122*, 7142–7152. doi: 10.1002/2017JA024126

Dubinin, E., Fraenz, M., Pätzold, M., Tellman, S., Woch, J., McFadden, J., & Zelenyi, L. (2021). Bursty ion escape fluxes at mars. *Journal of Geophysical Research: Space Physics*, *126*, e2020JA028920. doi: 10.1029/2020JA028920

Dudok de Wit, T., Kopp, G., Fröhlich, C., & Schöll, M. (2017). Methodology to create a new total solar irradiance record: Making a composite out of multiple data records. *Geophysical Research Letters*, *44*, 1196–1203. doi: 10.1002/2016GL071866

Eparvier, F. G., Chamberlin, P. C., Woods, T. N., & Thiemann, E. M. B. (2015). The solar extreme ultraviolet monitor for maven. *Space Science Reviews*, *195*, 293–301. doi: 10.1007/s11214-015-0195-2

Ergun, R. E., Andersson, L., Peterson, W. K., Brain, D., Delory, G. T., Mitchell, D. L., ... Yau, A. W. (2006). Role of plasma waves in mars' atmospheric loss. *Geophysical Research Letters*, *33*, L14103. doi: 10.1029/2006GL025785

Fowler, C., McFadden, J., Hanley, K., Mitchell, D., Curry, S., & Jakosky, B. (2022). In-situ measurements of ion density in the martian ionosphere: Underlying structure and variability observed by the maven-static instrument. *Journal of Geophysical Research: Space Physics*, *127*(8), e2022JA030352.

Halekas, J. (2017). Seasonal variability of the hydrogen exosphere of mars. *Journal of Geophysical Research: Planets*, *122*(5), 901–911.

Halekas, J. S., Ruhunusiri, S., Harada, Y., Collinson, G., Mitchell, D. L., Mazelle, C., ... Jakosky, B. M. (2017). Structure, dynamics, and seasonal variability of the mars-solar wind interaction: Maven solar wind ion analyzer in-flight performance and science results. *Journal of Geophysical Research: Space Physics*, *122*(1), 547–578. doi: 10.1002/2016JA023167

Halekas, J. S., Taylor, E. R., Dalton, G., Johnson, G., Curtis, D. W., McFadden, J. P., ... Jakosky, B. M. (2015). The Solar Wind Ion Analyzer for MAVEN. *Space Science Reviews*, *195*(1-4), 125–151. doi: 10.1007/s11214-013-0029-z

Hanley, K. G. (2023). *The beginnings of cold ion outflow at mars: Supply and energization near the exobase* (Unpublished doctoral dissertation). University of California, Berkeley.

Jakosky, B. M., & Phillips, R. J. (2001). Mars' volatile and climate history. *Nature*, *412*(6843), 237–244.

Lennartsson, O. W., Collin, H. L., & Peterson, W. K. (2004). Solar wind control of earth's h^+ and o^+ outflow rates in the 15-ev to 33-kev energy range. *Journal of Geophysical Research*, *109*(A12212). doi: 10.1029/2004JA010690

Lundin, R., Barabash, S., Fedorov, A., Holmström, M., Nilsson, H., & Sauvaud, J.-A. (2008). Solar forcing and planetary ion escape from mars. *Geophysical Research Letters*, *35*, L09203. doi: 10.1029/2007GL032884

Lundin, R., Zakharov, A., Pellinen, R., Barabash, S. W., Borg, H., Dubinin, E. M., ... N., P. (1990). Aspera/phobos measurements of the ion outflow from the martian ionosphere. *Geophysical Research Letters*, *17*, 873-876. doi: 10.1029/GL017i006p00873

Lundin, R., Zakharov, A., Pellinen, R., Borg, H., Hultqvist, B., N., P., ... Koskinen, H. (1989). First measurements of the ionospheric plasma escape from mars. *Nature*, *341*(6243), 609-612. doi: 10.1038/341609a0

Marquette, M. L., Lillis, R. J., Halekas, J. S., Luhmann, J. G., Gruesbeck, J. R., & Espley, J. R. (2018). Autocorrelation study of solar wind plasma and imf properties as measured by the maven spacecraft. *Journal of Geophysical Research: Space Physics*, *123*(4), 2493–2512.

McFadden, J. P., Kortmann, O., Curtis, D., Dalton, G., Johnson, G., Abiad, R., ... Jakosky, B. (2015). Maven suprathermal and thermal ion compostion (static) instrument. *Space Science Reviews*, *195*(1-4), 199–256. doi: 10.1007/s11214-015-0175-6

Nilsson, H., Carlsson, E., Brain, D. A., Yamauchi, M., Holmström, M., Barabash, S., ... Futaana, Y. (2010). Ion escape from mars as a function of solar wind conditions: A statistical study. *Icarus*, 40–49. doi: 10.1016/j.icarus.2009.03.006

Nilsson, H., Zhang, Q., Wieser, G. S., Holmström, M., Barabash, S., Futaana, Y., ... Wieser, M. (2021). Solar cycle variation of ion escape from mars. *Icarus*, 114610. doi: 10.1002/grl.50149

Pollack, J. B., Kasting, J. F., Richardson, S. M., & Poliakoff, K. (1987). The case for a wet, warm climate on early mars. *Icarus*, *71*(2), 203–224.

Ramstad, R., & Barabash, S. (2021). Do intrinsic magnetic fields protect planetary atmospheres from stellar winds? *Space Science Reviews*, *217*(2), 1-39.

Ramstad, R., Barabash, S., Futaana, Y., Nilsson, H., & Holmström, M. (2018). Ion escape from mars through time: An extrapolation of atmospheric loss based on 10 years of mars express measurements. *Journal of Geophysical Research: Planets*, *123*, 3051–3060. doi: 10.1029/2018JE005727

Ramstad, R., Barabash, S., Futaana, Y., Nilsson, H., Wang, X.-D., & Holmström, M. (2015). The martian atmospheric ion escape rate dependence on solar wind and solar euv conditions: 1. seven years of mars express observations. *Journal of Geophysical Research: Planets*, *120*(7), 1298–1309.

Schunk, R. W., & Nagy, A. F. (2009). *Ionospheres*. New York: Cambridge University Press.

Thiemann, E. M., Chamberlin, P. C., Eparvier, F. G., Templeman, B., Woods, T. N., Bougher, S. W., & Jakosky, B. M. (2017). The maven euvm model of solar spectral irradiance variability at mars: Algorithms and results. *Journal of Geophysical Research: Space Physics*, *122*(3), 2748–2767.

Wang, X.-D., Fatemi, S., Holmström, M., Nilsson, H., Futaana, Y., & Barabash, S. (2024). Martian global current systems and related solar wind energy transfer: Hybrid simulation under nominal conditions. *Monthly Notices of the Royal Astronomical Society*, *527*(4), 12232–12242.

Weber, T., Brain, D., Xu, S., Mitchell, D., Espley, J., Mazelle, C., ... Jakosky, B. (2021). Martian crustal field influence on o+ and o2+ escape as measured by maven. *Journal of Geophysical Research: Space Physics*, *126*(8), e2021JA029234.